Supporting Information for:

Interface-Enrichment-Induced Instability and Drug Loading-Enhanced-Stability in Inhalable Delivery of Supramolecular Filaments

Caleb F. Anderson,[†] Rami W. Chakroun, [†] Hao Su, [†] Roxana E. Mitrut, [†] Honggang Cui[†,‡,§]*

[†]Department of Chemical and Biomolecular Engineering and Institute for NanoBioTechnology, Johns Hopkins University, 3400 N Charles Street, Baltimore, Maryland 21218, United States

[‡]Department of Oncology and Sidney Kimmel Comprehensive Cancer Center, Johns Hopkins University School of Medicine, Baltimore, Maryland 21205, United States

[§]Center for Nanomedicine, The Wilmer Eye Institute, Johns Hopkins University School of Medicine, 400 North Broadway, Baltimore, Maryland 21231, United States

Corresponding Author Email: hcui6@jhu.edu

S1. Materials

All Fmoc amino acids and resins were purchased from Advanced Automated Peptide Protein Technologies (AAPPTEC, Louisville, KY). The oligoethylene glycol chain with carboxylic acid terminal ($mPEG_4$-CH_2CH_2COOH (OEG_5-COOH)) was purchased from PurePEG LLC (San Diego, CA). Paclitaxel was purchased from Ava Chem Scientific (San Antonio, TX). Coumarin 6 was acquired from Acros Organics (Fairlawn, NJ). Budesonide was sourced from TCI America (Portland, OR). All other reagents and solvents were sourced from VWR (Radnor, PA) or Sigma-Aldrich (St. Louis, MO).

S2. Peptide Synthesis and Purification

All peptide amphiphile molecules were synthesized with the standard 9-fluorenylmethoxycarbonyl (Fmoc) solid phase peptide synthesis technique. All three peptide amphiphiles (**EPA**, **OPA**, and **KPA**) were synthesized onto a Rink Amide MBHA resin. Fmoc deprotection was performed with 20% 4-methylpiperidine in dimethylformamide (DMF) for 15 minutes, repeated once. After Fmoc removal, each amino acid was conjugated onto the peptide chain at a 4:4:6 molar ratio of the Fmoc-amino acid, O-benzotriazole-N,N,N',N'-tetramehtyl-uronium-hexafluorophosphate (HBTU), and diisopropylethylamine (DIEA) to resin in DMF and allowed to react for 2 h. After last amino acid conjugation, lauric acid (C_{12} alkyl chain) was coupled to the peptide sequence in a 4:4:6 molar ratio to resin of lauric acid, HBTU, and DIEA in DMF and allowed to react overnight. For the **OPA** peptide, Mtt deprotection to lysine side chains was conducted with 3% trifluoroacetic acid (TFA) solution (5% triisopropylsilane (TIS), 92% dichloromethane (DCM)) for 10 min and repeated 5-6 times. OEG_5-COOH was coupled to the lysine side chains at a molar ratio of 2:2:3 to resin of OEG_5-COOH, HBTU, and DIEA. The completed PAs were cleaved from their resin by addition of a 10 mL mixture of 95% TFA, 2.5%

TIS, and 2.5% water and shaken for 3 h. After cleavage, the TFA solution containing PA was collected and precipitated with cold diethyl ether. After washing with diethyl ether, the crude PA precipitate was left under a fume hood to dry.

The crude PA solids were then dissolved in a water and acetonitrile (ACN) mixture containing 0/1% v/v TFA for **KPA** and **OPA** molecules and 0.1% v/v NH_4OH for **EPA**. A Varian ProStar Model 325 high performance liquid chromatography (HPLC) (Agilent Technologies, Santa Clara, CA) was used to purify the PA molecules using mobile phases of water and acetonitrile. Separation of PAs from impurities was performed using a Varian PLRP-S column (100 Å, 10 µm, 150 × 25 mm) with a flow rate of 20 mL/min, 10 mL injections, and monitoring at 220 nm for all molecules. For **EPA**, the gradient was run from 5% to 35% over 30 min; for **OPA**, the gradient was run from 20% to 65% ACN over 30 min; for **KPA**, the gradient was run from 20% to 50% ACN over 25 min. The collected fractions were analyzed by matrix-assisted laser desorption/ionization time of flight (MALDI-TOF) mass spectrometry to isolate the fractions containing the molecule of interest. The correct fractions were combined, and excess ACN was removed *via* rotary evaporation. Samples were then lyophilized using a FreeZone -105°C 4.5L freeze dryer (Labconco, Kansas City, MO). Re-characterization of the purified PA powders were conducted by RP-HPLC and MALDI-TOF, where PAs were calibrated, aliquoted into cryo-vials, and re-lyophilized. The purified powders were stored in a -20°C freezer for future use.[1–3]

S3. Matrix-Assisted Laser Desorption/Ionization Time of Flight Mass Spectrometry (MALDI-TOF)

The molecular weights of the synthesized PAs were determined using MALDI-TOF mass spectrometry with a BrukerAutoflex III MALDI-TOF instrument (Bruker, Billerica, MA). For sample preparation, 2 µL of sinapic acid matrix (10 mg/mL in 1:1 v/v water/ACN with 0.05% v/v

TFA; Sigma-Aldrich, St. Louis, MO) was deposited onto an MTP 384 ground steel target plate (Bruker, Billerica, MA). The matrix was allowed to dry for 5-10 min. After drying, 1 µL of aqueous PA solution was added to the corresponding spot of dried matrix followed by an immediate addition of 1 µL of sinapic matrix and mixed with the PA solution. The samples were allowed to dry for 10-20 min. In the instrument, the samples were irradiated with a 355 nm UV laser and analyzed in the reflectron mode. Representative mass spectra of the PAs are represented in **Figures S1-S3**.

S4. Analytical High Performance Liquid Chromatography (HPLC)

Analytical measurements with reverse-phase HPLC were performed with a Varian ProStar Model 325 HPLC (Agilent Technologies, Santa Clara, CA) using a Varian Pursuit XRs C18 column (5 µm, 150 × 4.6 mm) with a flow rate of 1 mL/min, 20 µL injections, and monitoring at 220 nm. The purity of the three PA molecules was confirmed using a gradient of 5% to 95% ACN over 15 min, where area under the curve (AUC) of the PA peak relative to total AUC of all peaks was used to confirm purity greater than 95%. The purity data for each molecule is shown in **Figure S1-3**. Calibration curves of the PA molecule concentrations were constructed by running different concentrations of the PAs at a gradient of 35% to 90% ACN over 15 min with monitoring at 280 nm (for tyrosine residue absorbance). The same gradient was used for calibration of the free drugs and dye studied in this work with monitoring at 237 nm for paclitaxel, 456 nm for coumarin 6, and 244 nm for budesonide. The AUC of the peak was plotted against the concentration, and the data fit with a linear regression.

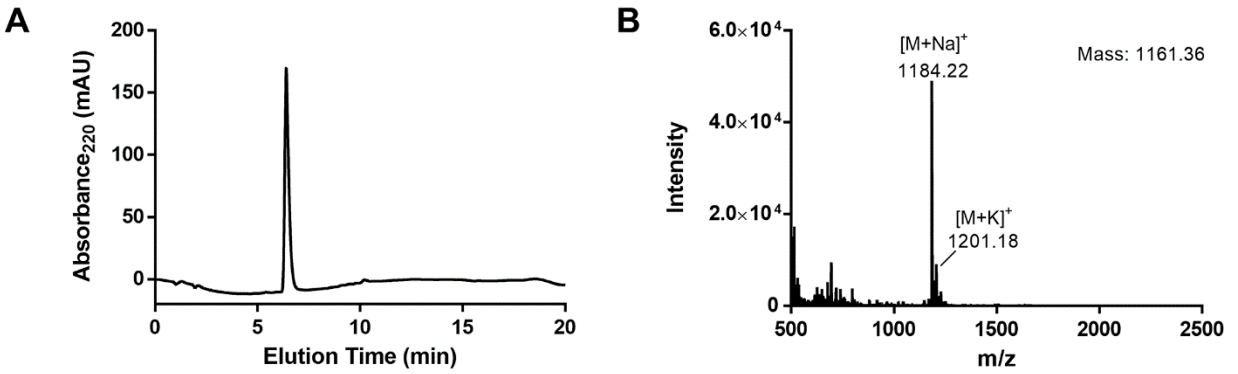

Figure S1. (A) Analytical RP-HPLC chromatogram and (B) MALDI-TOF mass spectrum of **EPA**.

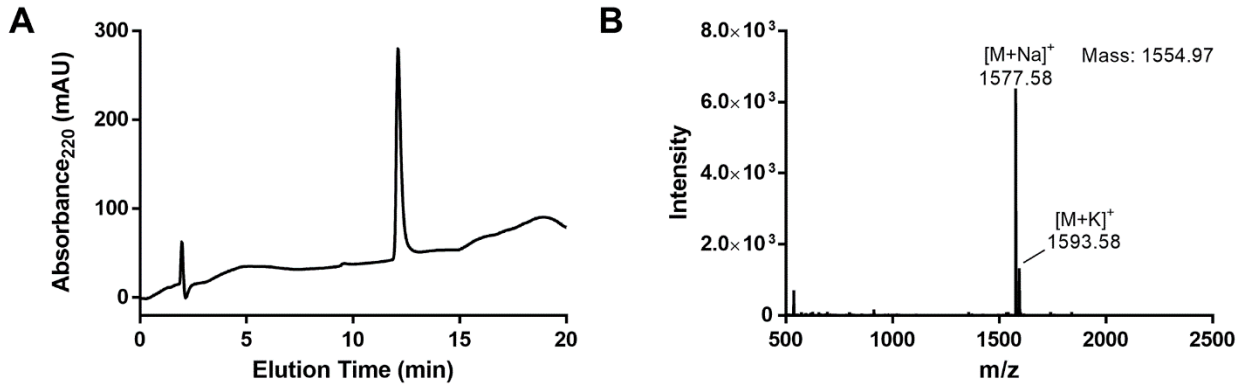

Figure S2. (A) Analytical RP-HPLC chromatogram and (B) MALDI-TOF mass spectrum of **OPA**.

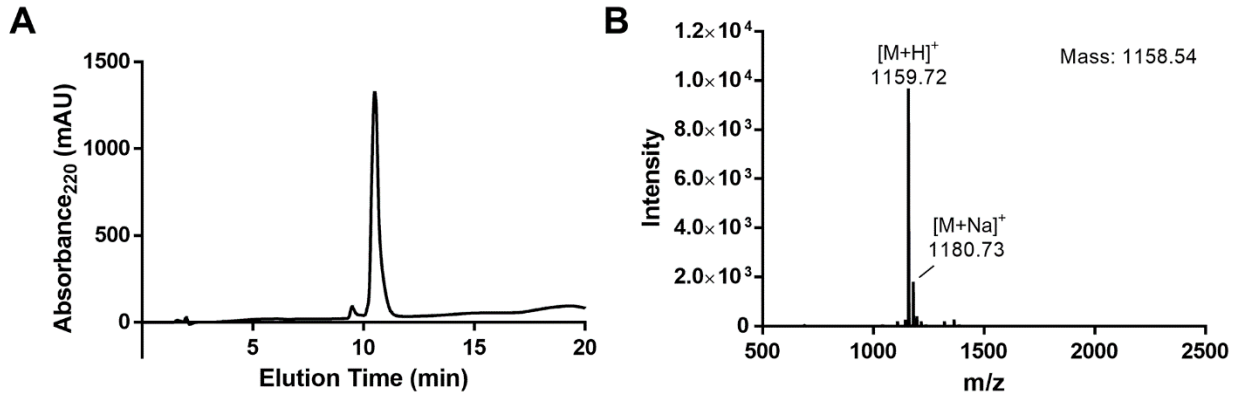

Figure S3. (A) Analytical RP-HPLC chromatogram and (B) MALDI-TOF mass spectrum of **KPA**.

S5. Zeta Potential Measurements

Solutions of the three PAs were dissolved in water and calibrated to pH = 7.4 using aqueous solutions of hydrochloric acid and sodium hydroxide. The solutions were allowed to age overnight at room temperature. The filament solutions were then added into a capillary cell and analyzed using a Malvern ZEN3690 Zetasizer (Malvern Panalytical, Westborough, MA) at 25°C. Three repeated measurements were performed for each sample (10 measurements/run) and then averaged. Zeta potential measurements of **EPA**, **OPA**, and **KPA** are displayed in **Figure S4**.

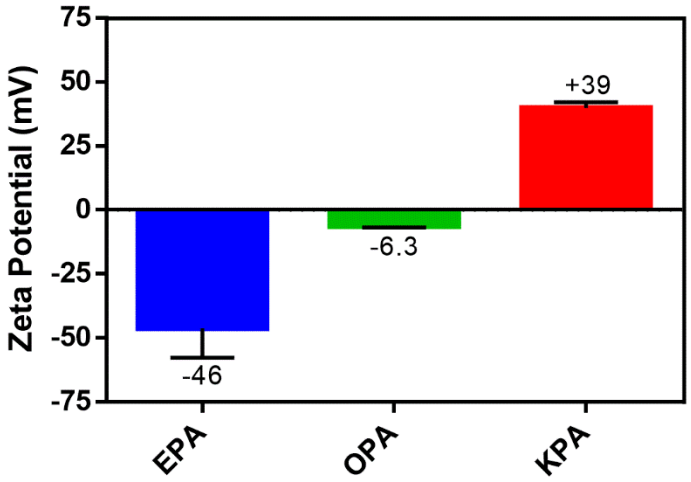

Figure S4. Zeta potential (mV) measurements of the three PA filament systems, confirming intended surface charge by molecular design of *C*-terminus amino acids of the PAs. Data are given as mean ± SD (n = 3).

S6. Transmission Electron Microscopy (TEM) Images of EPA, OPA, and KPA

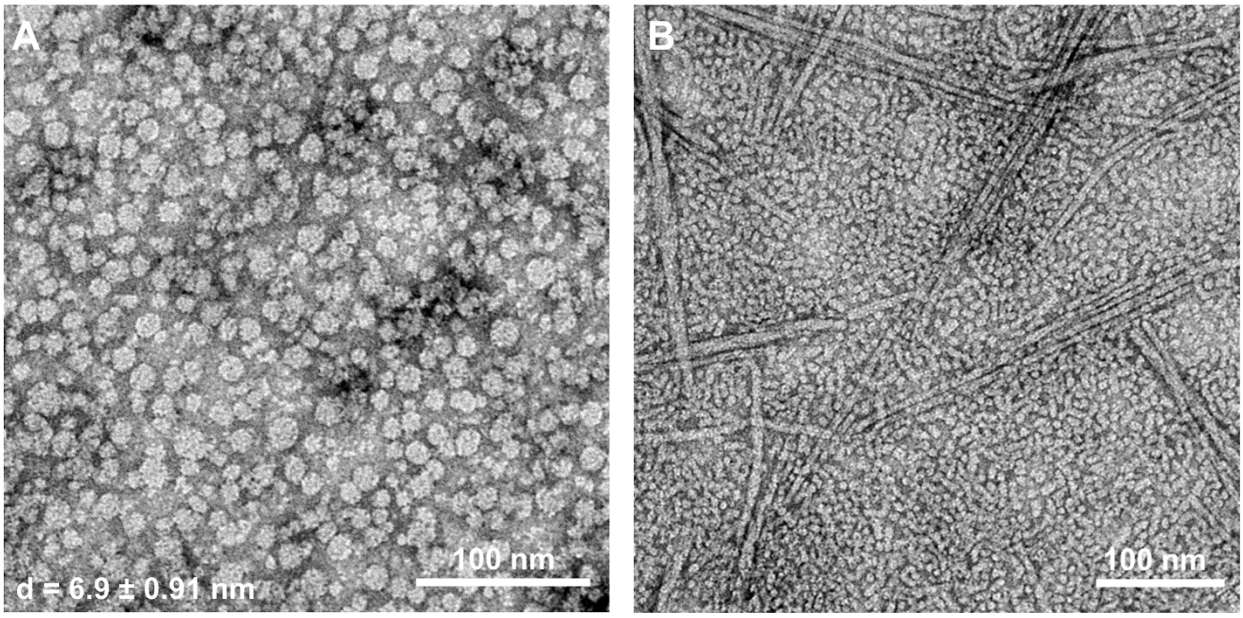

Figure S5. Representative TEM images of the formed spherical micelles resulting from jet nebulization (10 min) of **KPA** filamentsthat are present in the solutions of the (A) nebulized mist and (B) reservoir. Concentration of **KPA** is 500 µM in water. Diameter of the spherical micelles is given as mean ± SD (n = 35). Scale bars represent 100 nm.

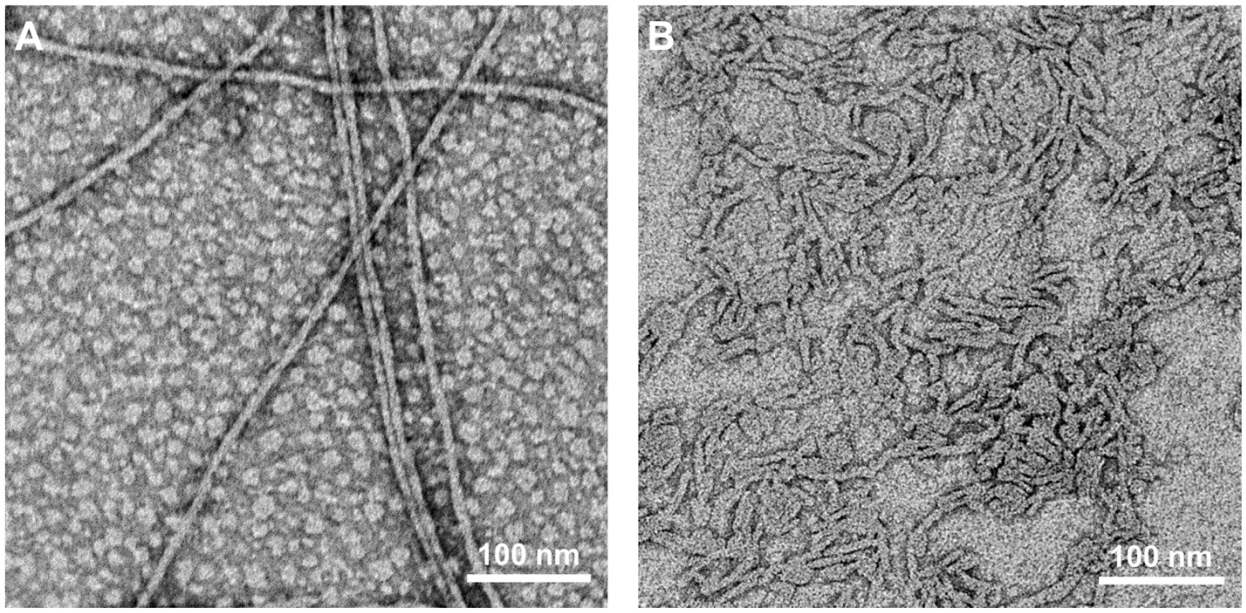

Figure S6. Representative TEM images of **KPA** filaments after dilution from 500 µM to 100 µM. (A) Spherical micelles are observed alongside the long filaments. Moreover, (B) worm-like micelles are also observed, suggesting the filament breakdown of **KPA** is reminiscent of a dilution effect.

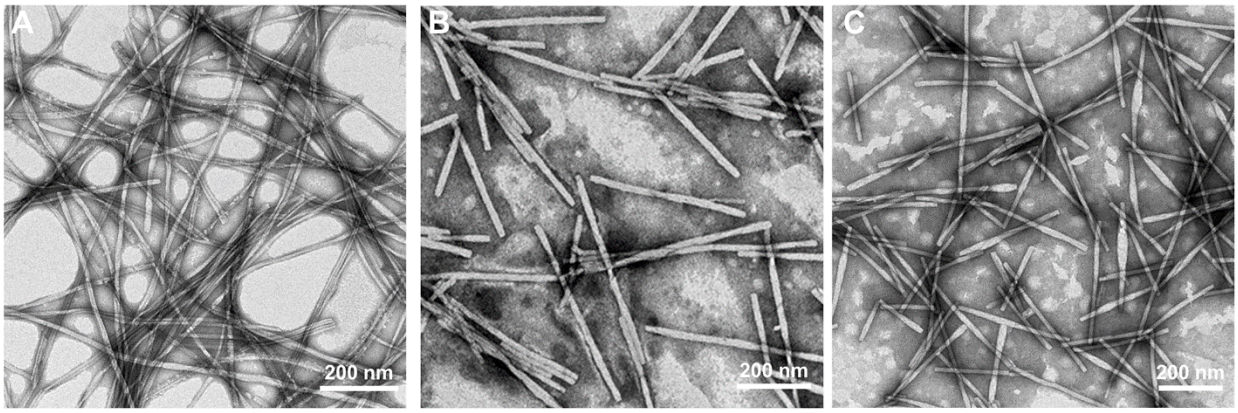

Figure S7. Representative low magnification TEM images of **EPA** filaments (A) before nebulization and after nebulization in the (B) nebulized mist and (C) reservoir. Filament solutions were nebulized at 500 µM in aqueous solution for 10 min. Scale bars represent 200 nm.

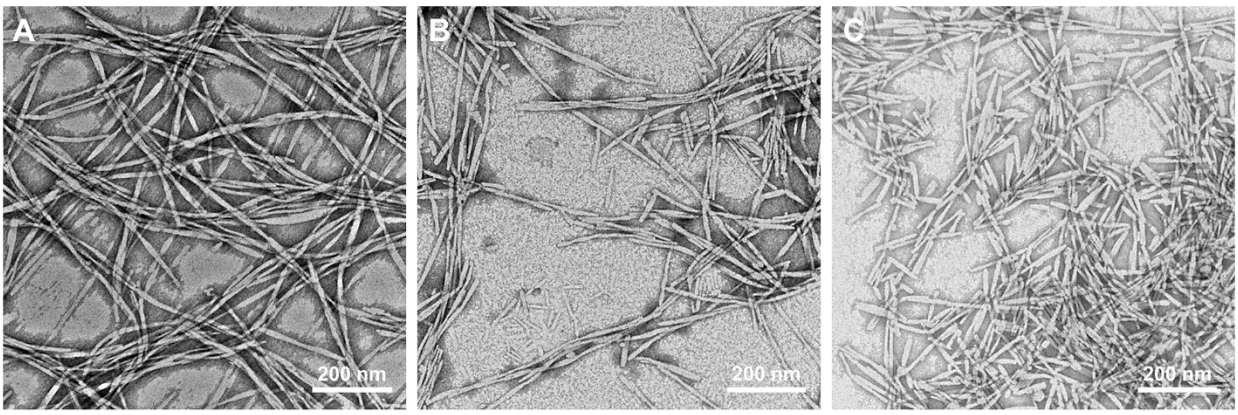

Figure S8. Representative low magnification TEM images of **OPA** filaments (A) before nebulization and after nebulization in the (B) nebulized mist and (C) reservoir. Filament solutions were nebulized at 500 µM in aqueous solution for 10 min. Scale bars represent 200 nm.

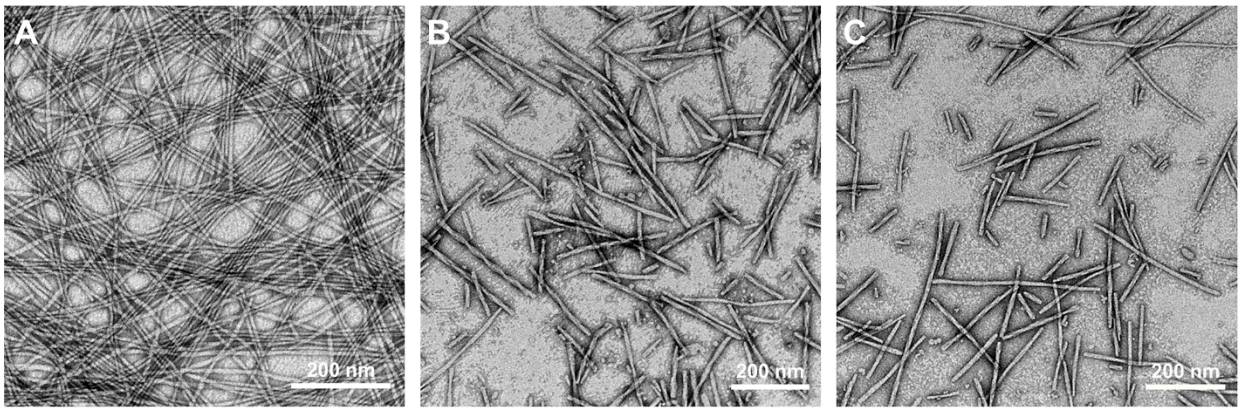

Figure S9. Representative low magnification TEM images of **KPA** filaments (A) before nebulization and after nebulization in the (B) nebulized mist and (C) reservoir. Filament solutions were nebulized at 500 µM in aqueous solution for 10 min. Scale bars represent 200 nm.

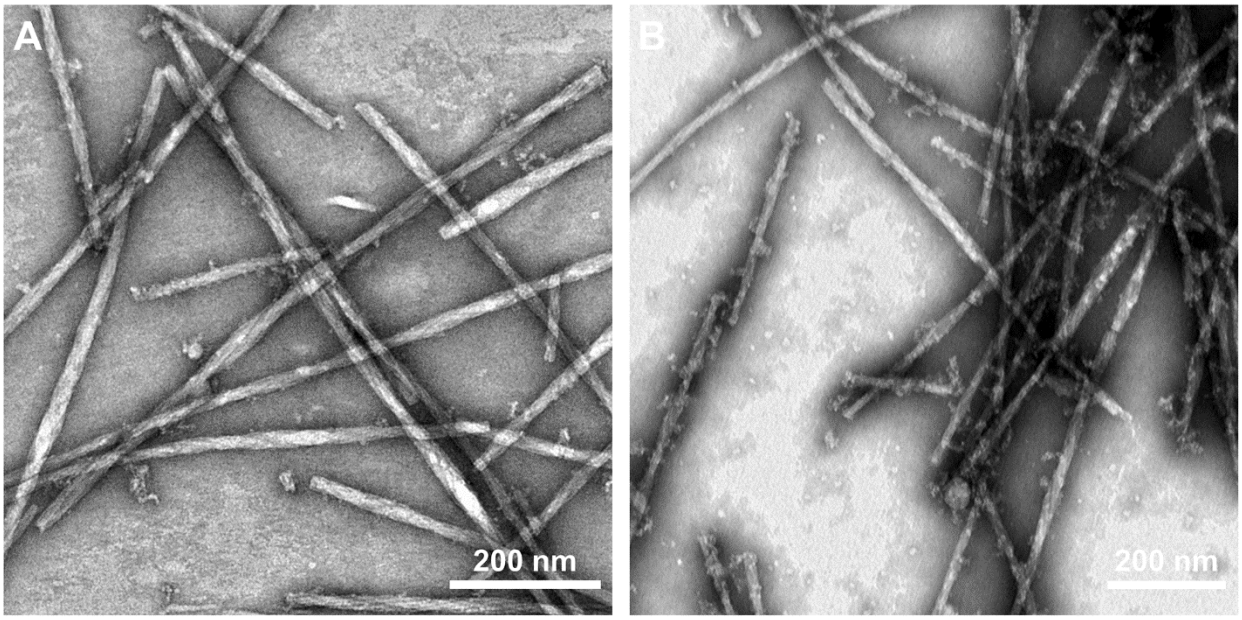

Figure S10. Representative TEM images of **EPA** filaments at 500 µM in aqueous solution after aging for 2 weeks after a 10 min nebulization event. Filaments from the (A) nebulized mist and (B) reservoir appear relatively unchanged compared to immediately after nebulization with the presence of some small aggregates. Scale bars are 200 nm.

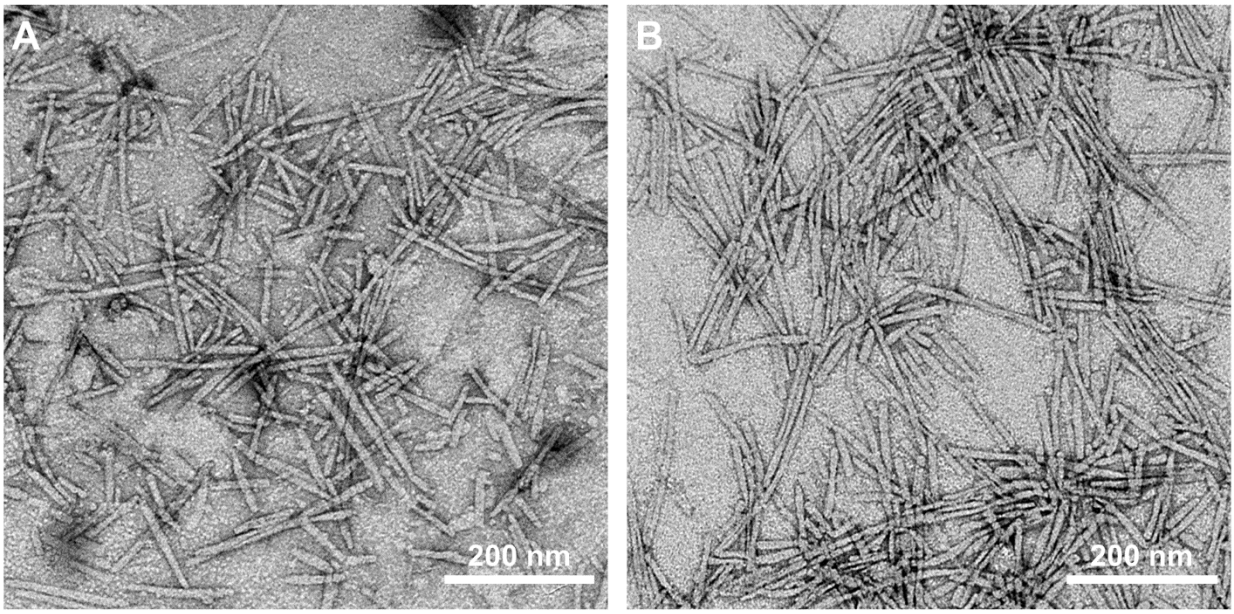

Figure S11. Representative TEM images of **OPA** filaments at 500 µM in aqueous solution after aging for 2 weeks after a 10 min nebulization event. Filaments from the (A) nebulized mist and (B) reservoir appear relatively unchanged compared to immediately after nebulization. Scale bars are 200 nm.

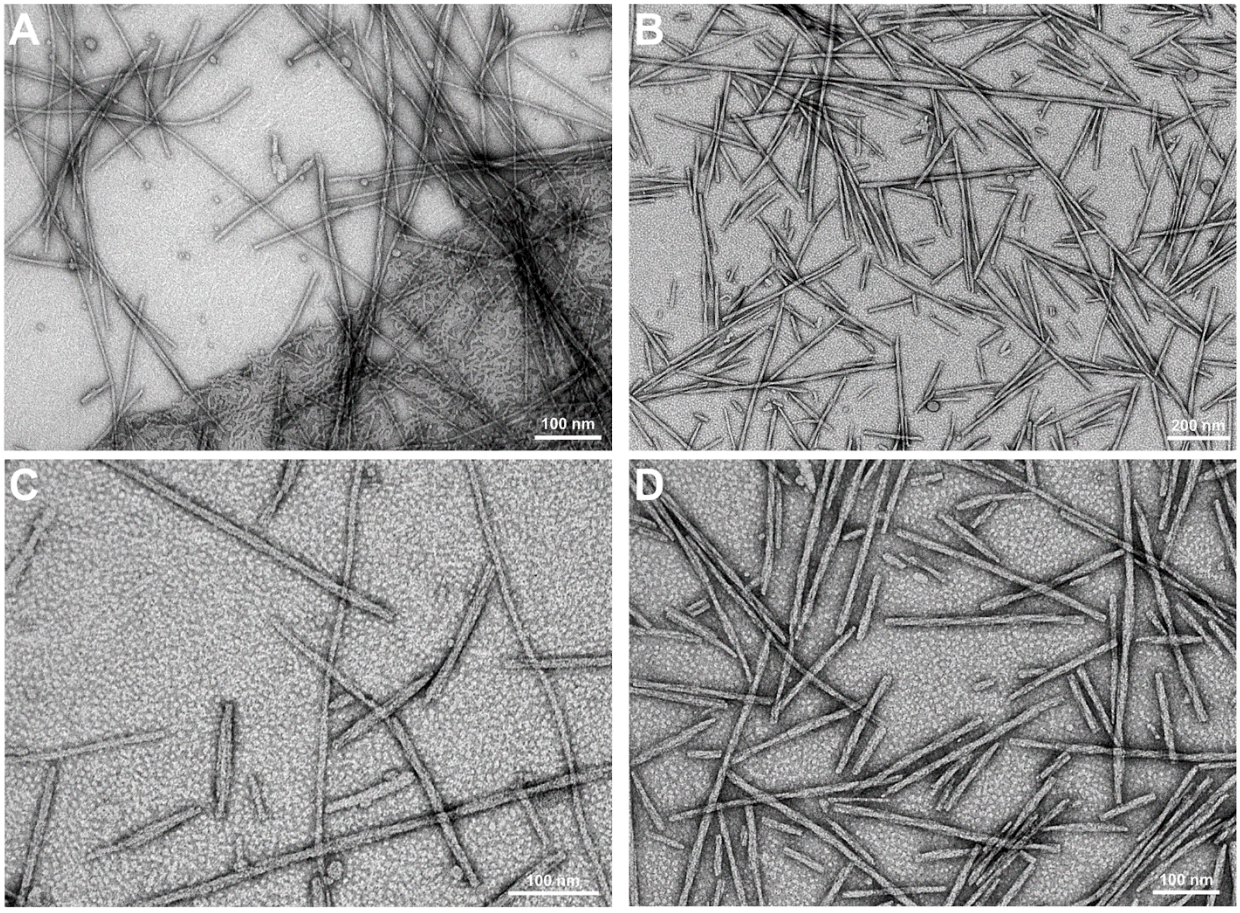

Figure S12. Representative TEM images of **KPA** filaments at 500 µM in aqueous solution after aging for 2 weeks after a 10 min nebulization event. Structures from the (A, C) nebulized mist and (B, D) reservoir appear relatively unchanged compared to immediately after nebulization. Lower magnification (A, B) and higher magnification (C, D) show the presence of the fibrils, worm-like micelles, and spherical micelles. Alongside the circular dichroism measurements (**Figure 4C**), the presence of these structures suggests nebulization induced a conformational change in assembly to a metastable state.

S7. Critical Assembly Concentration (CAC) Fluorescence Spectroscopy

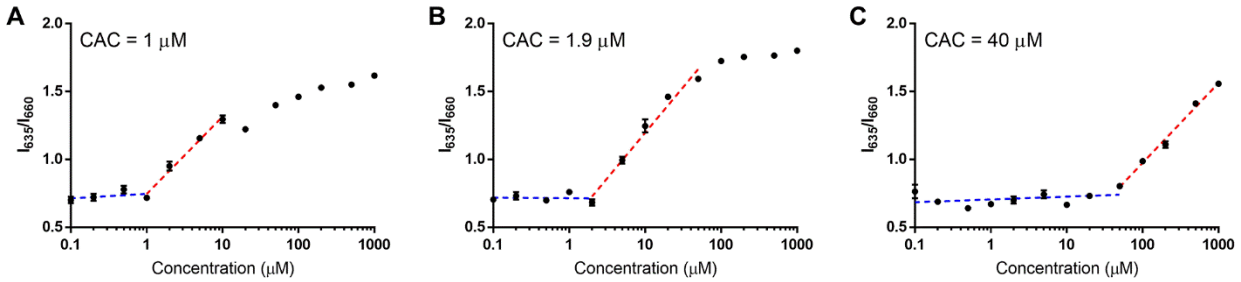

Figure S13. The critical assembly concentration (CAC) of (A) **EPA**, (B) **OPA**, and (C) **KPA** molecules in water as measure from a Nile Red Assay. Data presented in **Figure 5A-C** are also represented here but showing full range of concentrations tested from 0.1 µM to 2 mM.

S8. TEM Images of Drug/Dye-Loaded KPA Filaments

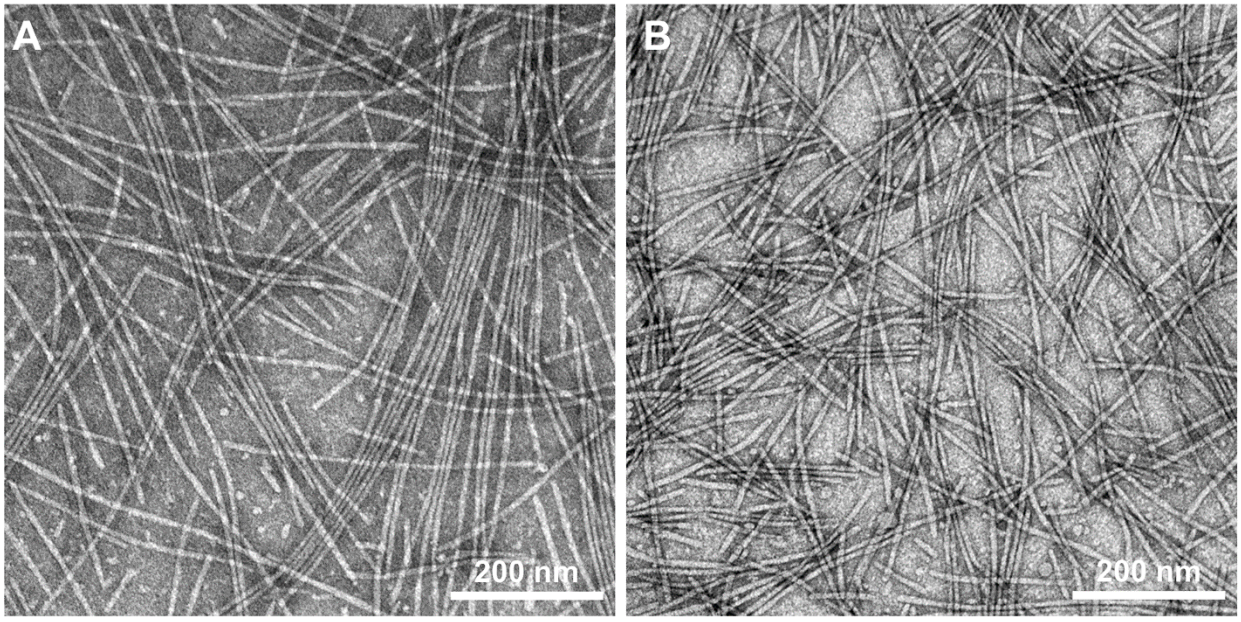

Figure S14. Representative low magnification TEM images of paclitaxel (PTX)-loaded **KPA** filaments at 500 μM in aqueous solution (A) before nebulization and (B) after nebulization in the emitted mist. Nebulization induces filament breakdown and spherical micelle formation, but encapsulation of the hydrophobic PTX mitigates the length reduction, suggesting the additional hydrophobic interaction stabilize the filamentous structures. Scale bars are 200 nm.

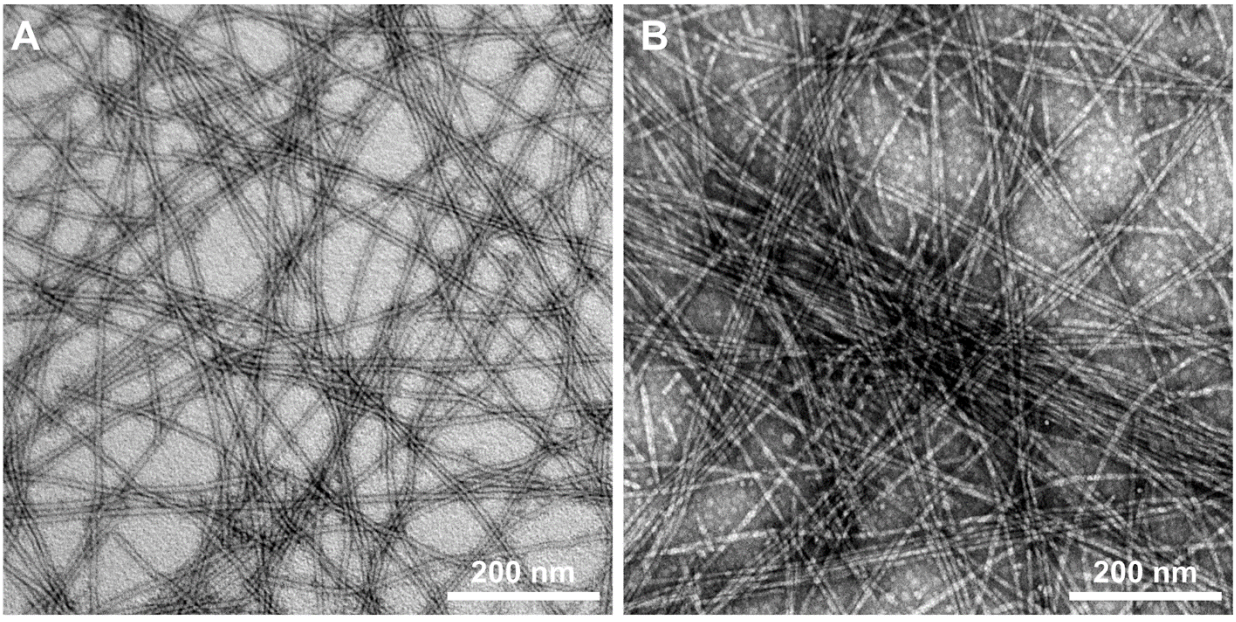

Figure S15. Representative low magnification TEM images of coumarin 6 (Cou6)-loaded **KPA** filaments at 500 μM in aqueous solution (A) before nebulization and (B) after nebulization in the emitted mist. Nebulization induces filament breakdown and spherical micelle formation, but encapsulation of the hydrophobic Cou6 mitigates the length reduction, suggesting the additional hydrophobic interaction stabilize the filamentous structures. Scale bars are 200 nm.

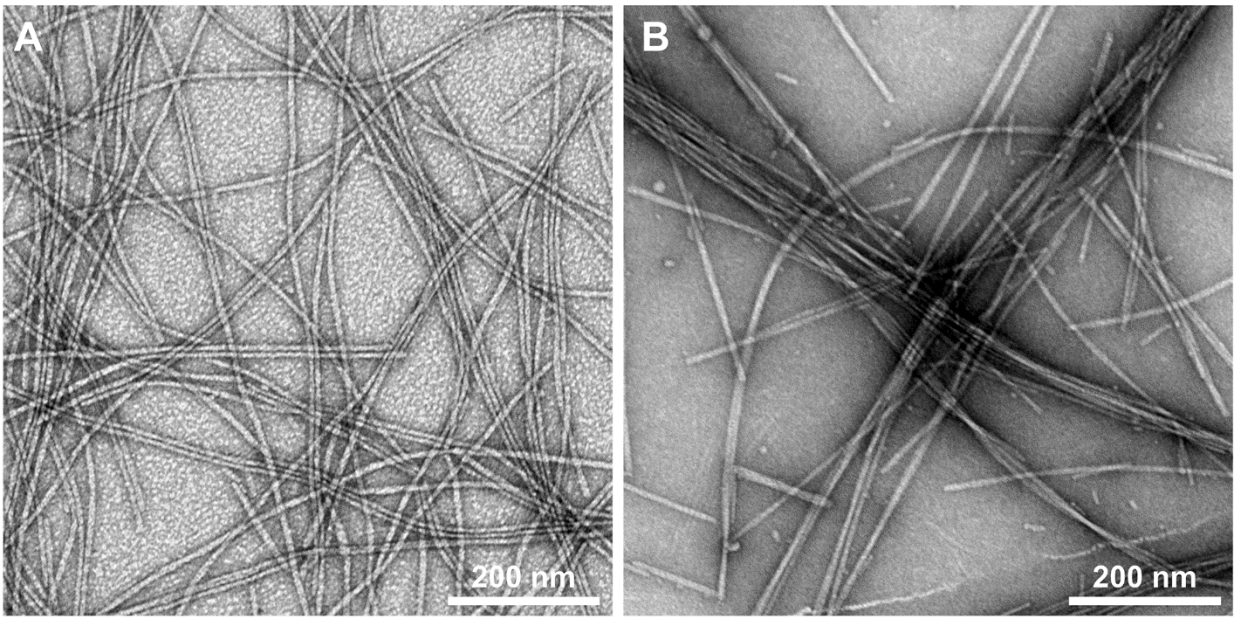

Figure S16. Representative low magnification TEM images of budesonide (BUD)-loaded **KPA** filaments at 500 µM in aqueous solution (A) before nebulization and (B) after nebulization in the emitted mist. Nebulization induces filament breakdown and spherical micelle formation, but encapsulation of the hydrophobic BUD mitigates the length reduction, suggesting the additional hydrophobic interaction stabilize the filamentous structures. Scale bars are 200 nm.

S9. Nebulizer Release Curves

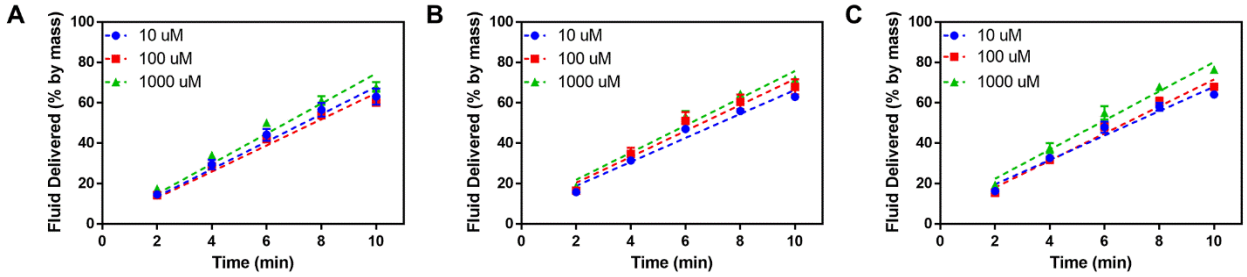

Figure S17. Fluid release from a jet nebulizer containing solutions of (A) **EPA**, (B) **OPA**, and (C) **KPA** filaments at various concentration (10 µM, 100 µM, and 1000 µM) over the course of a 10 min nebulization event. Fluid delivered represented as % by mass based on a starting volume of 3 mL in the reservoir of the device as determined *via* gravimetric analysis. Differences between formulation concentrations and molecular design are negligible, suggesting changes in surface and tension and viscosity between the concentrations are insignificant and the nebulizer device choice is likely the determining factor for fluid output. Data are given as mean ± SD (n = 3).

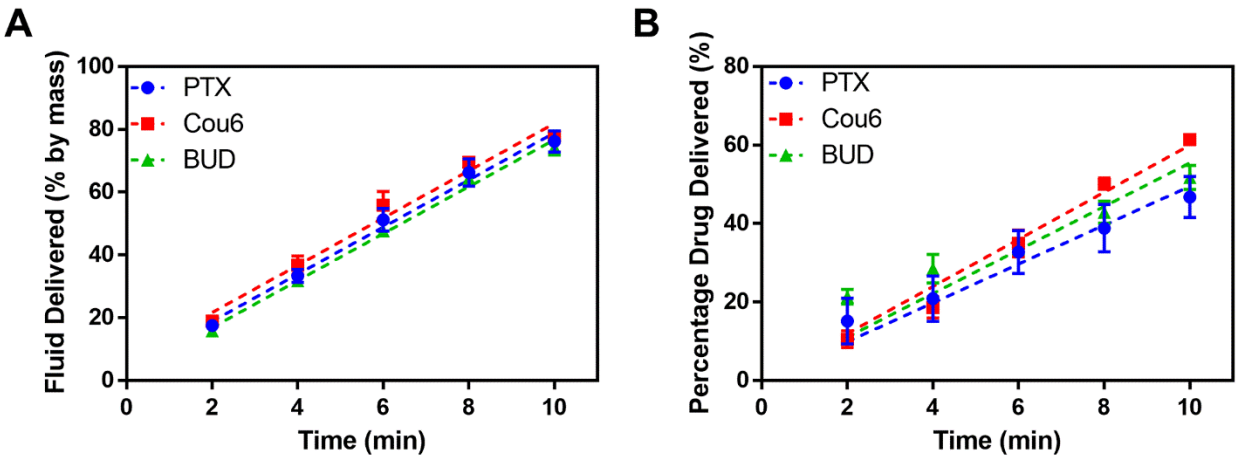

Figure S18. (A) The fluid release curve for the drug/dye-loaded **KPA** filaments at 1 mM in aqueous solution over the course of a 10 min nebulization event starting with 3 mL of solution in a jet nebulizer, showing negligible differences in fluid output (% by mass) between the different loading systems and thus further suggesting fluid output is likely device-dictated. (B) The total drug delivered from a jet nebulizer (% by mass) over the course of a 10 min nebulization event relative to the starting concentration of drug/dye within the **KPA** filaments. Differences between the different loading systems are negligible, further suggesting device choice is the critical factor in aerosol output. Differences in aerosol output between the fluid and the loaded drugs/dye suggests that concentration of the loaded moieties and their PA carrier varies amongst emitted droplets and thus filament output is nonhomogeneous over the course of a nebulization event. Data are given as mean ± SD (n = 3).

References

S1 Cheetham, A. G.; Zhang, P.; Lin, Y. A.; Lock, L. L.; Cui, H. Supramolecular Nanostructures Formed by Anticancer Drug Assembly. *J. Am. Chem. Soc.* **2013**, *135*, 2907–2910.

S2 Zhang, P.; Cheetham, A. G.; Lin, Y.-A.; Cui, H. Self-Assembled Tat Nanofibers as Effective Drug Carrier and Transporter. *ACS Nano* **2013**, *7*, 5965–5977.

S3 Lock, L. L.; Reyes, C. D.; Zhang, P.; Cui, H. Tuning Cellular Uptake of Molecular Probes by Rational Design of Their Assembly into Supramolecular Nanoprobes. *J. Am. Chem. Soc.* **2016**, *138*, 3533–3540.